An Efficient Methodology for the Analysis of Dielectric Shimming Materials in Magnetic Resonance Imaging

Jeroen Van Gemert,* Wyger Brink, Andrew Webb, and Rob Remis

***Abstract*— Interference effects in the transmit B_1^+ field can severely degrade the image quality in high-field Magnetic Resonance Imaging (MRI). High-permittivity pads are increasingly used to counteract these effects, but designing such pads is not trivial. In this paper, we present an efficient solution methodology for this dielectric RF shimming problem. By exploiting the fact that dielectric pads form a low rank perturbation of a large-scale background model, we are able to efficiently compute B_1^+ fields that correspond to a wide range of different pad realizations. This allows us to efficiently design dielectric pads that eliminate the B_1^+-interference effects of high-field MRI. We show that significant speed up factors can be achieved compared with traditional field simulation approaches and we validate our approach against measurements. Measured and simulated field responses are in good agreement with each other indicating that the proposed solution methodology enables us to efficiently analyze dielectric pads in realistic MRI measurement settings.**

***Index Terms*— B_1^+ fields, dielectric shimming, high-permittivity pads, magnetic resonance imaging, Sherman–Morrison–Woodbury formula.**

I. Introduction

CLINICAL Magnetic Resonance Imaging (MRI) is a well known noninvasive imaging modality to create detailed images of the human body. The generation of a high quality image can be extremely challenging, however, especially when imaging body parts that are large compared with the wavelength of the Radio-Frequency (RF) field. Constructive and destructive interference effects of the RF field can severely degrade the quality of an MR image reducing its use for interpretation and diagnostics [1], [2]. Interference effects may be particularly predominant for abdominal and cardiac imaging at 3T and neurological, abdominal, and cardiac imaging at 7T [3]– [6]. The corresponding RF frequencies for 3T and 7T are 128 MHz and 298 MHz, respectively. As an illustration, Figure 1 a shows the effects of interference in an head scan of a patient obtained with a 7T MRI system. Dark signal drop-outs or signal voids are clearly visible and certain parts of the anatomy can simply not be distinguished. Furthermore, the increased spatial variations in the RF excitation field may also lead to an increase of the local Specific Absorption Rate (SAR).

The RF excitation field is characterized by the forward circular polarized B_1^+ field, defined as

$$B_1^+ = \frac{B_x + jB_y}{2}, \tag{1}$$

where j is the imaginary unit, and B_x and B_y are the transverse x- and y-components of the frequency-domain magnetic flux density [7]. As is well known, this field flips the spins of the protons during an MRI experiment. Spatial inhomogeneities in the B_1^+ magnitude will therefore directly translate into spatial variations in the nutation of spins, and corresponding signal intensity in the final image.

RF shimming is a technique to tailor the RF field interference effects with the use of a transmit array or pTx (active shimming) or by using dielectric materials (passive shimming). Active shimming may require advanced coil designs and additional hardware. Dielectric shimming, on the other hand, makes use of high-permittivity dielectric pads which are relatively cheap to fabricate and can be readily integrated into the existing system architecture without any additional hardware [8].

The materials that are used for these pads typically have relative permittivity values of 80 and higher. In particular, calcium titanate powder mixed with deuterated water can be used if pads with a relative permittivity of about 110 are needed, while barium titanate powder mixed with water with a relative permittivity 300 is used if higher dielectric permittivities are required [9].

In practice, dielectric pads are placed in the vicinity of that part of the body to be imaged and a properly designed pad induces a secondary magnetic field that increases the signal in the regions of interest [10]– [16]. An example of the impact of a dielectric pad on the resulting MR image is illustrated in Figure 1 b, where a dielectric pad has been placed on the right side of the head. The signal drop-outs have been eliminated and detailed structures within the right hemisphere of the brain are now clearly visible. An additional advantage

Manuscript received September 16, 2016; revised October 22, 2016; accepted October 26, 2016. Date of publication November 2, 2016; date of current version February 1, 2017. The research reported in this paper is financially supported by the Dutch Technology Foundation (STW, project number 13375). *Asterisk indicates corresponding author.*

*J. Van Gemert is with the Circuits and Systems Group of the Electrical Engineering, Mathematics and Computer Science faculty, University of Technology Delft, Delft 2628 CD, The Netherlands.

W. Brink and A. Webb are with C. J. Gorter Center, Leiden University Medical Center, Leiden 2300 RC, The Netherlands.

R. Remis is with the Circuits and Systems Group of the Electrical Engineering, Mathematics and Computer Science faculty, University of Technology Delft, Delft 2628 CD, The Netherlands.

Digital Object Identifier 10.1109/TMI.2016.2624507

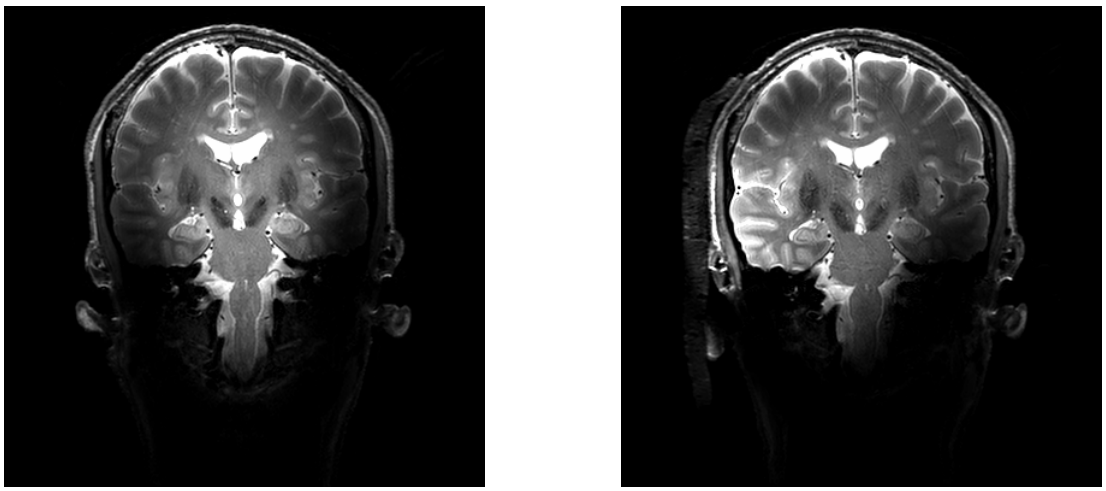

(a) (b)

Fig. 1. Head scan of a patient in a 7T (298 MHz) MRI system. (a) Signal drop-outs due to wavelength effects in a scan made without any dielectric pad. (b) Scan made with a dielectric pad on the right side of the head. The pad clearly resolves the signal-drop out problem in the right hemisphere of the brain. The pad that is used has a relative permittivity of about 300 with dimensions $18 \times 18 \times 1\text{cm}^3$. The scans have been acquired using a 7T Philips Achieva, where the head coil has been used for transmission and a 32-channel receive coil for reception. For this scan a T2-weighted turbo spin echo sequence has been used with an echo time of 44.8 ms, a pulse repetition time of 6300 ms, and a 120° refocusing pulse. 17 slices were acquired with a field-of-view of $107 \times 240 \times 198\ \text{mm}^3$. A parallel imaging acceleration factor of 1.5 has been used leading to a total scan time of 164 s.

of dielectric shimming is that the RF power required for excitation of the spins can be significantly reduced. In [17], for example, it is shown that by including dielectric pads in the MRI measurement setup, the RF power can be reduced by 50% while increasing the Signal-to-Noise ratio. Furthermore, dielectric pads do not influence the B_0 field distribution noticeably [13].

Designing optimal pads is a nontrivial task, however, since the homogeneity of the B_1^+ field is strongly dependent upon its parameters (location, constitution, and geometry). Pads are also patient specific and strongly depend upon the particular body part that is being imaged [18]. Furthermore, a straightforward design approach in which the B_1^+ field is determined for a range of pad parameters (so-called parameter sweeps) is far from practical, since for each realization the B_1^+ field inside the ROI needs to be computed using three-dimensional electromagnetic field solvers resulting in huge computational costs and computations that can even take days to complete.

In this paper, we propose a solution to this problem by computing the B_1^+ field in an efficient manner. This efficiency can be achieved by exploiting the fact that the dimensions of a dielectric pad are small compared with the dimensions of the background model (the body, RF shield, and RF coil). Specifically, since the body, the RF shield, and the RF coil remain fixed during pad design, we show that different pad realizations form low-rank perturbations of the background model. By computing and storing RF field responses in this background model during an offline stage, the RF fields resulting from a wide range of different pads (pads with different locations, sizes, and constitution) can be evaluated very efficiently during an online or design stage using the Sherman-Morrison-Woodbury formula [19]. By following this approach, significant speed-up factors can be achieved. In particular, for a realistic three-dimensional MRI imaging experiment of the human head, we show that speed-up factors ranging from 35 (for "large" pads) to 2000 (for "small" pads) can be achieved if we compare the computation times of our method with the time that is required to compute the RF field for each realization separately using FDTD. Furthermore, we also show that the Sherman-Morrison-Woodbury formula allows us to efficiently carry out a sensitivity analysis in which variations in the B_1^+ field due to variations in a pad (permittivity, geometry, etc.) can be determined. Finally, we validate our solution methodology by comparing computed B_1^+ fields with measured B_1^+ data *in vivo*.

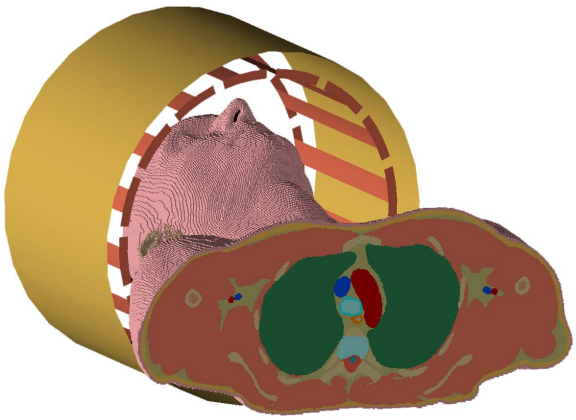

Fig. 2. The three-dimensional simulation setup used for 7T MRI imaging of the brain. The configuration consists of an RF shield, an RF coil, and a human body model.

II. Modeling Procedure for Dielectric Pads

As an illustrative example, we consider a typical MRI measurement setup in which the objective is to image an ROI

in the right hemisphere of the brain at 7T. The configuration of interest is illustrated in Figure 2 and consists of an RF shield, an RF coil, and a human body model. To compute the RF field in this configuration, we need to solve Maxwell's equations

$$-\nabla \times \mathbf{H} + \sigma \mathbf{E} + \mathrm{j}\omega\varepsilon\mathbf{E} = -\mathbf{J}^{\mathrm{ext}} \tag{2}$$

and

$$\nabla \times \mathbf{E} + \mathrm{j}\omega\mu\mathbf{H} = \mathbf{0}, \tag{3}$$

where $\mathbf{E}$ and $\mathbf{H}$ are the desired electric and magnetic field strengths and $\mathbf{J}^{\mathrm{ext}}$ is the external electric-current density describing the impressed current within an RF coil [20]. The conductivity, permittivity, and permeability within the domain of interest are given by σ, ε, and $\mu = \mu_0$, respectively, where μ_0 is the permeability of vacuum.

Given the complexity of this configuration, we can use a three-dimensional numerical solver to determine the RF fields. In practice, this amounts to solving the spatially discretized Maxwell system

$$(\mathsf{D} + \mathsf{N})\,\mathsf{f} = -\mathsf{q} \tag{4}$$

at a particular Larmor frequency ω [21]. In the above equation, D is the spatial differential operator containing the discretized curl operators occurring in Maxwell's equations and

$$\mathsf{N} = \mathsf{C} + \mathrm{j}\omega\mathsf{M} \tag{5}$$

is the medium matrix with C a medium matrix containing the conductivity values within the configuration and M a medium matrix containing the permittivity and permeability values within the computational domain. Furthermore, f is the field vector containing the components of the electric and magnetic field strength and q is a source vector containing the components of the external electric current densities as its elements. Finally, the order N of the discretized Maxwell system is equal to the total number of primary and dual grid edges in the computational domain [22]. We note that this order is typically very large especially for realistic three-dimensional configurations as considered here, usually it is in the order of 10^{6-7}. Directly solving the discretized Maxwell system for different medium matrices as is required when pads of different sizes and constitution are included can therefore be prohibitively expensive.

Dielectric pads are small compared to the dimensions of the computational domain, however, and inclusion of a dielectric pad therefore forms a small rank perturbation of the discretized Maxwell system of Eq. (4), since the position of the human body and the RF coil remain fixed. We take this observation into account by introducing the pad matrix

$$\mathsf{N}_{\mathrm{pad}} = \sum_{k\in\mathcal{P}} \left[\sigma_{\mathrm{pad}}(\mathbf{r}_k) + \mathrm{j}\omega\varepsilon_{\mathrm{pad}}(\mathbf{r}_k)\right] \mathsf{e}_k \mathsf{e}_k^T, \tag{6}$$

where $\mathcal{P} = \{k_1, k_2, \ldots, k_P\}$ is the index set of the pad, e_k is the kth canonical basis vector, $\mathbf{r}_k$ is the position vector of the kth grid edge that is occupied by the pad, and $\sigma_{\mathrm{pad}}(\mathbf{r}_k)$ and $\varepsilon_{\mathrm{pad}}(\mathbf{r}_k)$ are the conductivity and permittivity of the pad on the kth grid edge. The discretized Maxwell system for a configuration including a pad then becomes

$$\left(\mathsf{D} + \mathsf{N} + \mathsf{N}_{\mathrm{pad}}\right)\mathsf{f} = -\mathsf{q}. \tag{7}$$

We exploit the fact that the number of grid edges occupied by the pad P is much smaller than N to efficiently compute only the small rank perturbation of the system due to a dielectric pad by using the Sherman-Morrison-Woodbury formula (see [19], for example). To make this explicit, let us introduce the N-by-P pad support matrix S as

$$\mathsf{S} = \left[\mathsf{e}_{k_1}, \mathsf{e}_{k_2}, \ldots, \mathsf{e}_{k_p}\right] \tag{8}$$

and the reduced P-by-P pad matrix $\tilde{\mathsf{N}}_{\mathrm{pad}} = \mathrm{diag}(\mathsf{n})$ with its argument being a P-by-1 vector given by

$$\mathsf{n} = \left[\sigma_{\mathrm{pad}}(\mathbf{r}_{k_1}) + \mathrm{j}\omega\varepsilon_{\mathrm{pad}}(\mathbf{r}_{k_1}), \ldots, \sigma_{\mathrm{pad}}(\mathbf{r}_{k_P}) + \mathrm{j}\omega\varepsilon_{\mathrm{pad}}(\mathbf{r}_{k_P})\right]^T. \tag{9}$$

Here, the operation $\mathrm{diag}(\mathsf{n})$ constructs a square diagonal matrix with the elements of the vector n on its main diagonal. Using these definitions, we can also write $\mathsf{N}_{\mathrm{pad}} = \mathsf{S}\tilde{\mathsf{N}}_{\mathrm{pad}}\mathsf{S}^T$ and the discretized Maxwell system with pad included becomes

$$\left(\mathsf{A} + \mathsf{S}\tilde{\mathsf{N}}_{\mathrm{pad}}\mathsf{S}^T\right)\mathsf{f} = -\mathsf{q}, \tag{10}$$

where we have introduced the discretized Maxwell operator for a configuration without any pad as $\mathsf{A} = \mathsf{D} + \mathsf{N}$. Clearly, computing $\mathsf{f}^{\mathrm{no\ pad}} = -\mathsf{A}^{-1}\,\mathsf{q}$ amounts to determining the RF field in the case that no pad is present.

To find the RF field when a pad is present, we now formally solve Eq. (10) and apply the Sherman-Morrison-Woodbury formula. We obtain

$$\begin{aligned}\mathsf{f} &= -\left(\mathsf{A} + \mathsf{S}\tilde{\mathsf{N}}_{\mathrm{pad}}\mathsf{S}^T\right)^{-1}\mathsf{q} \\ &= \mathsf{f}^{\mathrm{no\ pad}} + \mathsf{Z}(\mathsf{I}_P - \tilde{\mathsf{N}}_{\mathrm{pad}}\mathsf{S}^T\mathsf{Z})^{-1}\tilde{\mathsf{N}}_{\mathrm{pad}}\mathsf{S}^T\mathsf{f}^{\mathrm{no\ pad}},\end{aligned} \tag{11}$$

where I_P is the identity matrix of order P and where we have introduced the so-called library matrix $\mathsf{Z} = -\mathsf{A}^{-1}\mathsf{S}$, which is a tall N-by-P matrix. Every column of S represents a unitary current forced on one edge of the pad domain, note that the birdcage does not act as a primary source in this case. The resulting fields in the domain of interest and the pad domain are stored in one column of matrix Z. We refer to this matrix as a library matrix, since it can be computed offline before any actual pad inclusion. The formula we presented here does not involve any approximations. However, the inverse in the formula should be non-singular, which is normally satisfied.

Equation (11) provides us with an explicit expression for all electric and magnetic field components on the entire domain of computation. To obtain the B_1^+ field values inside the head, we need to extract the relevant components from the field vector f. Suppose, for example, that the jth entry of the field vector f is equal to the x-component of the magnetic field strength at a particular location in a region of interest inside the head, while the kth entry of the field vector contains the y-component of the magnetic field strength at the same location. The B_1^+ field at this particular location of interest is then given by $B_1^+ = \mathsf{r}^T\mathsf{f}$, where r is the recorder vector for the location of interest given by

$$\mathsf{r} = \frac{\mu_0}{2}(\mathsf{e}_j + \mathrm{j}\,\mathsf{e}_k). \tag{12}$$

The B_1^+ field inside an entire region of interest can be obtained from the field vector by introducing a recorder vector for each location. Storing these recorder vectors as columns in the N-by-N_r recorder matrix R, where N_r is the total number of locations inside the region of interest, the B_1^+ field inside this region is obtained as

$$\mathsf{b}_1^+ = \mathsf{R}^T \mathsf{f}. \tag{13}$$

Substituting Eq. (11) into the above equation, we arrive at

$$\mathsf{b}_1^+ = \mathsf{b}_1^{+;\text{no pad}} + \mathsf{R}^T \mathsf{Z}(\mathsf{I}_P - \tilde{\mathsf{N}}_\text{pad}\mathsf{S}^T\mathsf{Z})^{-1}\tilde{\mathsf{N}}_\text{pad}\mathsf{S}^T\mathsf{f}^{\text{no pad}}, \tag{14}$$

where $\mathsf{b}_1^{+;\text{no pad}} = \mathsf{R}^T\mathsf{f}^{\text{no pad}}$ is the B_1^+ field inside the region of interest in the case that there is no pad present.

The main advantage of using the above formulation is that as soon as the library matrix Z is available, the B_1^+ field response to a wide variety of dielectric pads can be computed very efficiently, since for each particular pad only the second term in Eq. (14) needs to be evaluated. In fact, Eq. (14) suggests that we can split the design procedure for dielectric pads into an offline stage and online design stage. During the offline stage, we first identify a pad design domain that surrounds the particular part of the body to be imaged. This domain consists of all grid edges that can be occupied by a pad and we subsequently construct the library matrix Z for the selected pad design domain. As soon as the library matrix is available, we start the online design stage by computing the B_1^+ field using Eq. (14). We note that when the dimensions of the evaluated pad are smaller than that of the pad design space, we can further reduce the order of our system by including only the relevant columns of the support matrix S and library matrix Z. Therefore, the evaluation of the second term amounts to solving a system of at most order P and, as pointed out above, this order is much smaller than the order N of the total system. Consequently, we can very efficiently evaluate different RF fields due to a wide variety of pads with different shapes and constitution. Moreover, since $P \ll N$ direct solvers can often even be used and this has the additional advantage that the computation time required to determine the scattered fields due to the presence of a pad becomes independent of the contrast of a pad.

To summarize, we propose the following RF field modeling procedure to compute electromagnetic fields in dielectric shimming:

1) Offline stage
   - For a given part of the human body in which the electromagnetic field is required, first compute the $\mathsf{b}_1^{+;\text{no pad}}$ field and the field $\mathsf{f}^{\text{no pad}}$, which are the fields in absence of any dielectric pad.
   - Identify a pad design domain where a pad can be positioned.
   - Construct the library matrix Z by filling its columns one by one, that is, compute $\mathsf{Z}(:,k) = -\mathsf{A}^{-1}\mathsf{e}_{k_p}$ for all $k_p \in \mathcal{P}$. Here e_{k_p} is one of the columns of our support matrix S. In our case we solve this system using a commercial FDTD solver since this is known to solve electromagnetic problems efficiently, although other methods are possible as well. If $\mathsf{Z}(:,k)$ is computed using an iterative solver, then $\mathsf{Z}(:,k-1)$ may serve as an initial guess.
2) Online stage
   - Compute the B_1^+ field for a pad of any desired shape or constitution using Eq. (14). For a pad covering P grid edges, only a small P-by-P system needs to be solved. A particular pad should be located within the preallocated pad domain, of course, since this domain determines the columns of matrix S.

In Section IV we illustrate the performance of this solution procedure and compare the computed B_1^+ fields with measurements as well.

III. Sensitivity Analysis

The RF field changes at a particular location within the human body when a pad is included in the background configuration, or when the shape, location, or constitution of the dielectric pad changes. To investigate these effects, we carry out a sensitivity analysis using the Sherman-Morison-Woodbury expression for the RF field as given by Eq. (11). This expression allows us to explicitly compute the Jacobian of the field with respect to changes in the shape, location, and contrast of the pad. In particular, writing $\mathsf{b}_1^+ = \mathsf{b}_1^+(\mathsf{n})$ for the field as given by Eq. (14), we have

$$\mathsf{b}_1^+(\mathsf{n}+\delta\mathsf{n}) \approx \mathsf{b}_1^+(\mathsf{n}) + \mathsf{J}(\mathsf{n})\,\delta\mathsf{n} \tag{15}$$

for a sufficiently small contrast perturbation vector $\delta\mathsf{n}$, where J is the Jacobian given by

$$\mathsf{J}(\mathsf{n}) = \mathsf{R}^T\mathsf{Z}(\mathsf{I}_P - \tilde{\mathsf{N}}_\text{pad}\mathsf{S}^T\mathsf{Z})^{-1}\,\mathrm{diag}(w_1, w_2, \ldots, w_m) \tag{16}$$

with $w_m = \mathsf{e}_{k_m}^T\mathsf{f}(\mathsf{n})$ for $m = 1, 2, \ldots, P$. The perturbation vector $\delta\mathsf{n}$ allows us to change the properties of the pad. We observe that with the library matrix Z at our disposal, again only a small system of order P has to be solved to determine the first-order variations in the field due to changes in contrast function values of the pad. This allows us to efficiently carry out a pad sensitivity analysis.

Moreover, the availability of the Jacobian also enables us to carry out full nonlinear Gauss-Newton-type minimization schemes for optimal dielectric pad design, see e.g. [23]. Although this will be something for future work, a first step towards pad design could be to describe a desired B_1^+ field and define a cost function as

$$C(\mathbf{n}) = \|\mathsf{b}_1^+(\mathsf{n}) - \mathsf{b}_1^{+;\text{desired}}\|_2^2.$$

This cost function can be minimized for a particular pad (n) in an iterative fashion by linearizing $\mathsf{b}_1^+(\mathsf{n})$ and solving the normal equations to find an update direction. Specifically, having a current reconstruction n_i available, a new reconstruction is computed via the update direction $\mathsf{n}_{i+1} = \mathsf{n}_i + \delta\mathsf{n}$, where

$$\delta\mathsf{n} = \left[\mathsf{J}^H(\mathsf{n}_i)\mathsf{J}(\mathsf{n}_i)\right]^{-1}\mathsf{J}^H(\mathsf{n}_i)\epsilon(\mathsf{n}_i). \tag{17}$$

Here $\epsilon(\mathsf{n}_i) = \mathsf{b}_1^+(\mathsf{n}_i) - \mathsf{b}_1^{+;\text{desired}}$ denotes the error of the desired field with respect to the field obtained with a pad for iteration i.

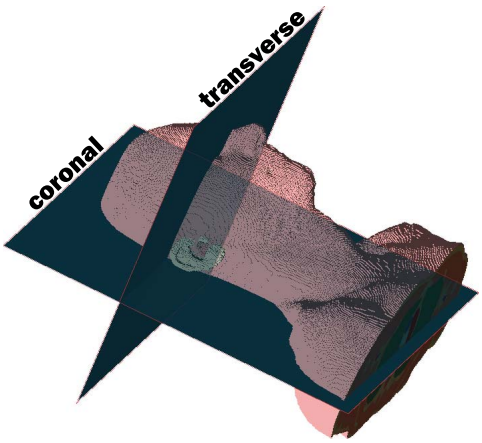

Fig. 3. Coronal and transverse slices through the head used to depict the B_1^+ fields.

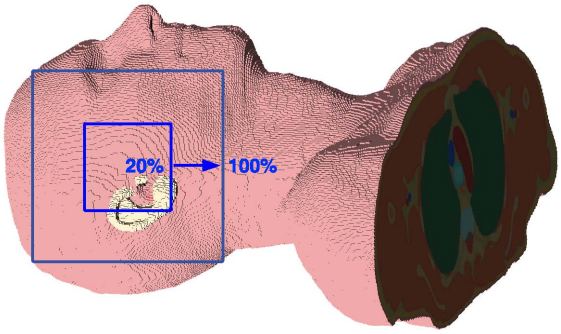

Fig. 4. Pad design domain of $18 \times 18 \times 1$ cm^3 located on the right-hand side of the human head. The domain has a thickness of 1 cm. Pad sizes range from 100% (the pad design domain is completely filled) to 20%. All pads are centered around the midpoint of the pad design domain.

IV. Simulations and Measurements

We illustrate the performance of our dielectric shimming procedure by evaluating the design of dielectric pads for 7T MR imaging of a local ROI in the right hemisphere of the brain. The simulated configuration is depicted in Figure 2 and consists of the head and shoulders of the male body model "Duke" from the Virtual Family dataset [24], a 7T 16-rung high-pass birdcage coil with a radius of 15 cm operating in quadrature mode at 298 MHz, and an RF shield with a radius of 18 cm. The configuration has a 5 mm^3 resolution. The coronal and transverse slices used to depict the B_1^+ fields inside the head are shown in Figure 3.

In the offline stage of our solution procedure, we first compute the fields $\mathsf{b}_1^{+;\text{no pad}}$ and $\mathsf{f}^{\text{no pad}}$. Figure 7 (left column) shows the magnitude of this B_1^+ field within the transverse and coronal slices. Interference effects of the 298 MHz RF field at 7T are responsible for the signal drops on the left and right-hand side of the head. The fields are computed by Remcom XFdtd software (v.7.5.0.3, State College, PA, USA). The computational domain in XFdtd consists of nearly 10^6 grid edges and we have set the stopping criteria of the simulations to -40 dB convergence.

Having the background field available, we now have to identify a pad design domain. Since the objective of the MRI

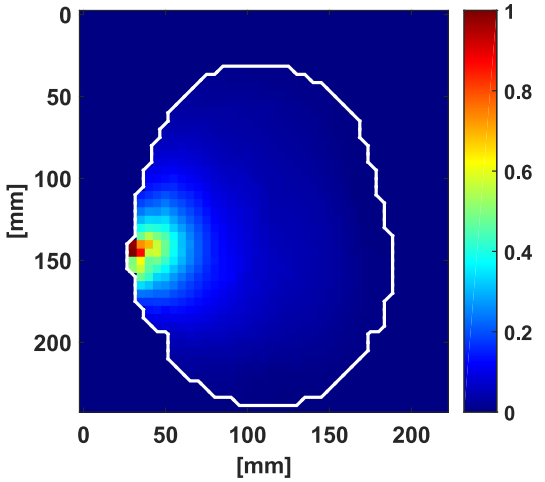

Fig. 5. Normalized sensitivity of the B_1^+ field inside the head with respect to changes in a single grid edge located within the pad domain. This grid edge has been indicated with the arrow.

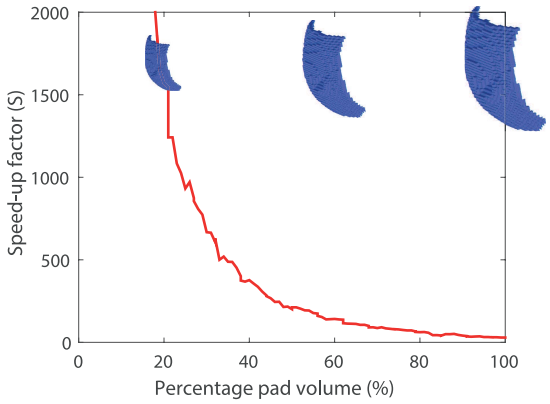

Fig. 6. Speed-up factors for concentric square pads with increasing volumes. The pad volume ranges from 20% of the volume of the preassigned pad domain to 100% of the pad domain (pad domain is completely filled).

experiment is to image an ROI in the right hemisphere of the brain, we define a pad design domain of $18 \times 18 \times 1$ cm^3 on the right side of the head as indicated by the outer square area in Figure 4. The thickness of the design domain is taken to be 1 cm to comply with typical thicknesses of pads used to image parts of the human head. Subsequently, the library matrix Z is constructed using Remcom's XFdtd software. To investigate in which areas the B_1^+ field can be affected by a dielectric pad, we now first carry out a sensitivity analysis using the Jacobian of Eq. (16). Specifically, we select a particular grid edge in the pad domain (the pth grid edge, say) and determine the normalized sensitivity of the B_1^+ field inside the head by computing the pth column of the Jacobian and normalizing this column with respect to the entry with the largest absolute value. Figure 5 shows the magnitude of the sensitivity of the B_1^+ field with respect to changes in the indicated pad grid edge. This result clearly shows that the B_1^+ field can indeed be affected by placing a dielectric pad on the right-hand side of the head. Sensitivity analyses for other pad grid edges can be carried out in a similar manner.

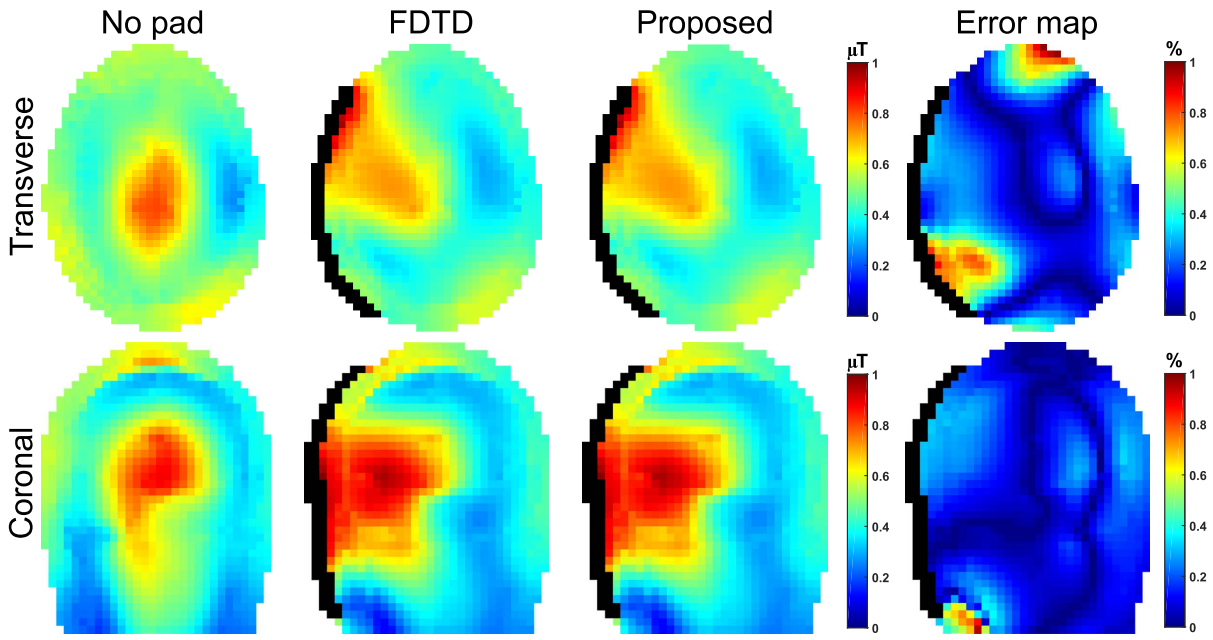

Fig. 7. Magnitude and error map of the B_1^+ field in the coronal and transverse slices through the head. Left column: magnitude of the $B_1^{\mathcal{C}}$ field without any pad, second column: B_1^+ field as computed by Remcom's XFdtd, third column: magnitude of the $B_1^{\mathcal{C}}$ field as computed by the proposed solution procedure, right column: relative error map of the $B_1^{\mathcal{C}}$ field in percent. The dielectric pad is indicated in black and has a permittivity of 285 ε_0 F/m and a conductivity of 0.25 S/m.

To illustrate the efficiency of the proposed method, and to illustrate that the degree of efficiency depends on the dimensions of the pads, we compute the B_1^+ fields for a series of pads with different sizes. Specifically, we start with a pad that completely occupies the pad design domain and subsequently reduce its size down to 20% of the volume of the original full-sized pad (see Figure 4). For simplicity, we consider homogeneous pads only and fix the dielectric properties of the pad ($\varepsilon_{\text{pad}} = 285\varepsilon_0$ F/m, $\sigma_{\text{pad}} = 0.25$ S/m), but we stress that our formulation allows for inhomogeneous pads with varying medium parameters as well (see Section II).

To indicate what speed up factors can be achieved with our approach, we compare the CPU time t_1 required by Remcom's XFdtd package to compute the B_1^+ field for a particular pad with the CPU time t_2 needed by the online stage of the design procedure as proposed in this paper. Specifically, for a particular pad the speed up factor is defined as $S = t_1/t_2$. All CPU times are measured on a Windows 64-bit machine with an Intel Xeon CPU X5660 @ 2.80 GHz (dual core) with 48 GB internal memory and two NVIDIA Tesla K40c GPU's.

Figure 6 shows the speed up factor for a series of concentric dielectric pads with increasing volumes. For the smallest pad with a volume of 20% of the volume of the total preassigned pad domain, the proposed method is approximately 2000 times faster than XFdtd. The speed up factor clearly decreases as the volume of the pad increases and we end up with a speed up factor of 35 for a pad that completely fills the pad domain (CPU times $t_1 = 300$ s and $t_2 = 8.5$ s). To illustrate the effectiveness in similar configurations, the work presented in [25] where two pads with dimensions $10 \times 14 \times 1$ cm^3 are used would have been computed in 6 s ($S = 50$). And the work presented in [26] where three pads with dimensions $7 \times 7 \times 0.5$ cm^3 are used would have been computed in 0.3 s ($S = 1000$). These large speed up factors can be achieved since we computed the library matrix Z beforehand during the offline stage of our solution procedure. For the realistic 3D background model considered in this experiment (see Fig 2), we constructed almost 6000 library vectors stored as columns in matrix Z, where each vector results from one column of our support matrix S (see Section II). This process takes approximately 26 hours on the above mentioned machine when computed using the GPU, but as soon as it is available for a fixed background consisting of the human body, RF coil, and RF shield, it allows for very efficient pad design and B_1^+ fields corresponding to a wide variety of pads of different sizes and constitution can be determined in a very efficient manner.

Finally, we validate our design procedure by comparing the simulated B_1^+ field with direct XFdtd computations and measurements. The second and third column of Figure 7 show the magnitude of the B_1^+ field in the coronal and transverse plane as computed by XFdtd and the proposed solution procedure for a pad that completely occupies the pad design domain ($\varepsilon_{\text{pad}} = 285\varepsilon_0$ F/m, $\sigma_{\text{pad}} = 0.25$ S/m). The exact location of the pad has been indicated in Figure 7. The right column of Figure 7 shows the relative error map in percent. The field computed directly by XFdtd and the field computed using Eq. (14) essentially coincide, since Eq. (14) is an identity. However, we do see some small errors in the error map, most of them are located in the low field areas in the vicinity of the dielectric pad. This is for some part expected, since the

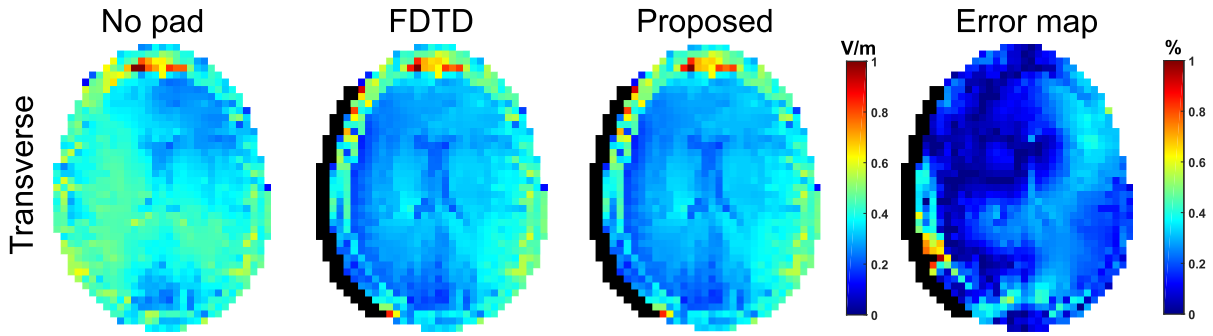

Fig. 8. Magnitude and error map of the electric field in the transverse slice through the head. Left column: magnitude of electric field without any pad, second column: magnitude of the electric field as computed by Remcom's XFdtd in V/m, third column: magnitude of the electric field as computed by the proposed solution procedure in V/m, right column: relative error map of the electric field in percent. The dielectric pad is indicated in black and has a permittivity of 1000 ε_0 F/m and a conductivity of 2.5 S/m.

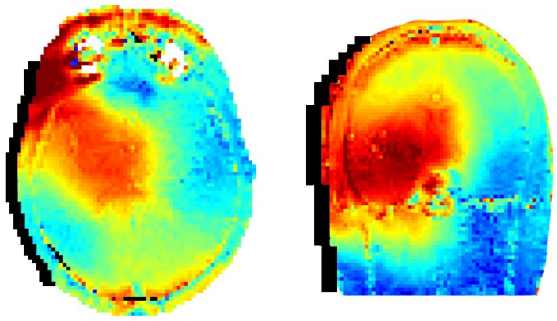

Fig. 9. Magnitude of the measured B_1^+ field (*in vivo*) for a dielectric pad (indicated in black) with a permittivity of 285 ε_0 F/m and a conductivity of 0.25 S/m. Left column depicts the field for the transverse slice and the right column depicts the field for the coronal slice.

relative error is depicted. Remaining differences between the methods may arise from the finite convergence time used to construct the library matrix Z, which then causes small errors to accumulate globally. Nevertheless, the differences remain very small (at most 1%). Furthermore, Figure 9 shows the measured B_1^+ map obtained *in vivo* for the dielectric pad used in the simulations. The map was obtained using a DREAM B_1^+ mapping sequence with a 2.5 mm^2 resolution [27], a 5 mm slice thickness and preparation and imaging flip angles of 50° and 10°, respectively. The measured B_1^+ maps are clearly in good agreement with the simulated B_1^+ maps and the destructive interference effect at the right-hand side of the head has been reduced significantly due to the application of the dielectric pad. Discrepancies between the measured data and simulated data arise from modeling errors that are common in both simulation methods (different body model, position of the body model, pad position, etc.) and are not related to the proposed solution method.

To show that our method holds for other constitutions of the pad as well, we take some unusual high values for the conductivity and permittivity, i.e. $\sigma_{\text{pad}} = 2.5$ S/m and $\varepsilon_{\text{pad}} = 1000\varepsilon_0$ F/m. In Figure 8 the magnitude of the electric fields are shown for a transverse slice of the head when computed with FDTD (second column) and with our proposed method (third column). The relative error map is shown in the right column where we see that the introduced errors are still very small.

V. Conclusion and Discussion

In this paper, we have presented an efficient forward modeling methodology for the efficient design of dielectric pads in MRI. During the design procedure, the background consisting of the RF shield, coil, and human body do not change, while the dimensions of the dielectric pads are small compared to the dimensions of the background model. Consequently, the pads form a small rank perturbation of the computational domain and the resulting RF fields can be efficiently determined by exploiting the well-known Sherman-Morrison-Woodbury formula. We stress that this formula is an identity and hence does not involve any approximations, provided that the inverse that we need to compute does exist. Our numerical experiments show that by following this approach, significant speed-up factors can be achieved compared with straightforwardly computing the RF field for each pad realization. Obviously, when the pad becomes excessively large the method might be less efficient since this would not yield a small rank perturbation with respect to the computational domain. However, such configurations are not realistic since dielectric pads are typically small compared to the human subject. Furthermore, we have validated our methodology by comparing predicted B_1^+ fields with full FDTD solutions and measurements carried out on a male human head. The simulated and measured field responses are in good agreement with each other, illustrating that the proposed solution methodology allows for effective pad analysis in dielectric shimming.

In our present implementation, the background model is subject dependent and different libraries have to be used for different subjects (male, female, etc.). In practice, a quick survey scan of the patient will allow us to select a library that fits best with the posture of the patient. In future work, we will investigate to what extent it is possible to construct patient independent body models (or models that are suitable for a particular class of patients) by applying homogenization or more general model-order reduction techniques to the body models [28]. These techniques can reduce the number of libraries, thereby reducing the computational costs of the

offline stage of our solution procedure. These computational costs can also be reduced by relaxing the convergence settings of the FDTD solver used for calculating these libraries, which in this work has been chosen conservatively.

Additionally, we are planning to combine our proposed solution methodology with fully nonlinear optimization schemes (Newton- or Gauss-Newton schemes, for example) to find optimal dielectric pads that minimize a differentiable objective function that measures the discrepancy between a desired and a modeled B_1^+ field as described briefly in Section III.

Finally, our method not only determines the magnetic field strength but also the electric field strength, the SAR within the body can be efficiently computed for a complete range of different pad designs of interest as well. More generally, the method can be fruitfully applied in any MRI setting in which electrically small materials or devices are included. The possible appearance of hotspots around implants such as deep brain stimulators, for example, could effectively be studied using our approach. With our proposed solution methodology, RF fields and derived quantities such as the SAR can be computed very efficiently for a wide range of devices or pads so long as these devices are electrically small and form a low rank perturbation of a fixed and large-scale background model.

ACKNOWLEDGMENT

The authors thank Prof. Alexander Yarovoy of the Microwave Sensing, Systems and Signals group of Delft University of Technology for many discussions and support.

REFERENCES

[1] M. A. Bernstein, J. Huston, and H. A. Ward, "Imaging artifacts at 3.0 T," *J. Magn. Reson. Imag.*, vol. 24, no. 4, pp. 735–746, 2006.

[2] J. K. Chang and I. R. Kamel, "Abdominal imaging at 3 T: Challenges and solutions," *Appl. Radiol.*, vol. 39, no. 10, p. 22, 2010.

[3] K. Sung and K. S. Nayak, "Measurement and characterization of RF nonuniformity over the heart at 3T using body coil transmission," *J. Magn. Reson. Imag.*, vol. 27, no. 3, pp. 643–648, 2008.

[4] O. Dietrich, M. F. Reiser, and S. O. Schoenberg, "Artifacts in 3-T MRI: Physical background and reduction strategies," *Eur. J. Radiol.*, vol. 65, no. 1, pp. 29–35, 2008.

[5] J. T. Vaughan *et al.*, "7T vs. 4T: RF power, homogeneity, and signal-to-noise comparison in head images," *Magn. Reson. Med.*, vol. 46, no. 1, pp. 24–30, 2001.

[6] P. F. van de Moortele *et al.*, "B_1 destructive interferences and spatial phase patterns at 7 T with a head transceiver array coil," *Magn. Reson. Med.*, vol. 54, no. 6, pp. 1503–1518, 2005.

[7] D. I. Hoult, "The principle of reciprocity in signal strength calculations—A mathematical guide," *Concept. Magn. Res.*, vol. 12, no. 4, pp. 173–187, 2000.

[8] S. A. Winkler and B. K. Rutt, "Practical methods for improving B_1^+ homogeneity in 3 Tesla breast imaging," *J. Magn. Reson. Imag.*, vol. 41, no. 4, pp. 992–999, 2015.

[9] W. M. Teeuwisse, W. M. Brink, K. N. Haines, and A. G. Webb, "Simulations of high permittivity materials for 7 T neuroimaging and evaluation of a new barium titanate-based dielectric," *Magn. Reson. Med.*, vol. 67, no. 4, pp. 912–918, 2012.

[10] W. M. Brink and A. G. Webb, "A forward model analysis of dielectric shimming in magnetic resonance imaging," in *Proc. Int. Conf. Electromagn. Adv. Appl. (ICEAA)*, Sep. 2013, pp. 528–531, doi: 10.1109/iceaa.2013.6632294.

[11] W. M. Brink, A. M. A. van der Jagt, M. J. Versluis, B. M. Verbist, and A. G. Webb, "High permittivity dielectric pads improve high spatial resolution magnetic resonance imaging of the inner ear at 7 T," *Invest. Radiol.*, vol. 49, no. 5, pp. 271–277, 2014.

[12] W. M. Brink, R. F. Remis, and A. G. Webb, "A theoretical approach based on electromagnetic scattering for analysing dielectric shimming in high-field MRI," *Magn. Reson. Med.*, vol. 75, no. 5, pp. 2185–2194, May 2016, doi: 10.1002/mrm.25783.2015.

[13] W. M. Teeuwisse, W. M. Brink, and A. G. Webb, "Quantitative assessment of the effects of high-permittivity pads in 7 Tesla MRI of the brain," *Magn. Reson. Med.*, vol. 67, no. 5, pp. 1285–1293, 2012.

[14] P. de Heer, W. M. Brink, B. J. Kooij, and A. G. Webb, "Increasing signal homogeneity and image quality in abdominal imaging at 3 T with very high permittivity materials," *Magn. Reson. Med.*, vol. 68, no. 4, pp. 1317–1324, 2012.

[15] P. de Heer, M. B. Bizino, H. J. Lamb, and A. G. Webb, "Improved cardiac proton magnetic resonance spectroscopy at 3 T using high permittivity pads," *Invest. Radiol.*, vol. 51, no. 2, pp. 134–138, 2016.

[16] Q. X. Yang *et al.*, "Manipulation of image intensity distribution at 7.0 T: Passive RF shimming and focusing with dielectric materials," *J. Magn. Reson. Imag.*, vol. 24, no. 1, pp. 197–202, 2006.

[17] Q. X. Yang, J. Wang, J. Wang, C. M. Collins, C. Wang, and M. B. Smith, "Reducing SAR and enhancing cerebral signal-to-noise ratio with high permittivity padding at 3 T," *Magn. Reson. Med.*, vol. 65, no. 2, pp. 358–362, 2011.

[18] W. M. Brink and A. G. Webb, "High permittivity pads reduce specific absorption rate, improve B_1 homogeneity, and increase contrast-to-noise ratio for functional cardiac MRI at 3 T," *Magn. Reson. Med.*, vol. 71, no. 4, pp. 1632–1640, 2014.

[19] G. H. Golub and C. F. van Loan, *Matrix Computations*, 4th ed. Baltimore, MD, USA: Johns Hopkins Univ. Press, 2012, p. 65.

[20] A. T. De Hoop, *Handbook of Radiation and Scattering of Waves*. London, U.K.: Academic, 1995.

[21] U. S. Inan and R. A. Marshall, *Numerical Electromagnetics: The FDTD Method*, 1st ed. Cambridge, U.K.: Cambridge Univ. Press, 2011, p. 352.

[22] A. Taflove and K. R. Umashankar, "The finite-difference time-domain method for numerical modeling of electromagnetic wave interactions," *Electromagnetics*, vol. 10, nos. 1–2, pp. 105–126, 1990.

[23] S. Boyd and L. Vandenberghe, *Convex Optimization*. Cambridge, U.K.: Cambridge Univ. Press, 2004, ch. 9.

[24] A. Christ, "The virtual family–development of surface-based anatomical models of two adults and two children for dosimetric simulations," *Phys. Med. Biol.*, vol. 55, no. 2, pp. N23–N38, 2010.

[25] J. E. M. Snaar *et al.*, "Improvements in high-field localized MRS of the medial temporal lobe in humans using new deformable high-dielectric materials," *NMR Biomed.*, vol. 24, no. 7, pp. 873–879, 2011.

[26] K. R. O'Brien *et al.*, "Dielectric pads and low-B_1^+ adiabatic pulses: Complementary techniques to optimize structural T_1w whole-brain MP2RAGE scans at 7 Tesla," *J. Magn. Reson. Imag.*, vol. 40, no. 4, pp. 804–812, 2014.

[27] K. Nehrke and P. Börnert, "DREAM—A novel approach for robust, ultrafast, multislice B_1 mapping," *Magn. Reson. Med.*, vol. 68, no. 5, pp. 1517–1526, 2012.

[28] A. C. Antoulas, *Approximation of Large-Scale Dynamical Systems*. Philadelphia, PA, USA: SIAM, 2005.